Available online at www.sciencedirect.com

jmr&t Journal of Materials Research and Technology

journal homepage: www.elsevier.com/locate/jmrt

Original Article

JMAK model applied on the κ-carbide precipitation in FeMnAlC steels

Carlo Mapelli [a], Giacomo Villa [a,*], Silvia Barella [a], Andrea Gruttadauria [a], Davide Mombelli [a], Xavier Veys [b], Lode Duprez [b]

[a] Dipartimento di Meccanica – Politecnico di Milano, Via La Masa 1, 20156, Milano, Italy
[b] ArcelorMittal Global R&D, OCAS NV, Technologiepark 48 BE, Zwijnaarde, 9052, Gent, Belgium

ARTICLE INFO

Article history:
Received 28 June 2021
Accepted 29 September 2021
Available online 4 October 2021

Keywords:
κ-carbide
Precipitation
Low density steels
Lightweight steels
JMAK

ABSTRACT

Different lightweight steels alloys have been treated by different isothermal treatments in order to understand the basics of precipitation kinetics of κ-carbide for such class of new steel grades featured by high concentration of Mn and Al. The κ-carbide precipitation plays a significant role to induce the strengthening of these steel grades that maintain a significant ductility up to the fracture as a consequence of their duplex ferrite-austenite structure that exploits the twinning mechanism of austenite during the plastic deformation. In this paper the results about isothermal transformations involving the κ-carbide precipitation have been discussed.

In order to deepen the comprehension of the mechanisms involved in precipitation of κ-carbides, the study has been performed by isothermal (Temperature Transformation Treatment) experiments applying different temperatures and holding times. The observed transformations have been measured and it has been possible to apply the JMAK model to fit such results. In addition, it has been observed a relationship between the steel composition and the activation energy for the transformation.

1. Introduction

In recent years, the awareness about global climate change has risen in all the sectors, even in steel making [1] and transportation industry [2–4]. Considering that 20% of the of energy consumption and CO_2 emission are globally generated from the transportation sector [1,3], particular attention was given to the possibility to decrease the vehicles weight in order to reduce the vehicles fuel consumption and so their CO_2 emissions [2–5]. Advantages are presents also for electric vehicles as vehicles light-weighting could increase their battery range, decreasing their energy demand [4]. In order to reach this objective, the vehicle manufactures can approach the problem in three way: (1) optimize the component design, (2) use high strength steels (or even more performing materials) and reduce the weight by having thinner components or (3) use materials with lower density and optimize the weight reduction with the necessary resisting cross section [1].

Considering the possibility to take advantage of a material with both lightness and high strength characteristics, lightweight steels are now deeply studied because of their

* Corresponding author.
E-mail address: giacomo.villa@polimi.it (G. Villa).
https://doi.org/10.1016/j.jmrt.2021.09.139

interesting combination of mechanical properties. First of all, the steel density can be easily 10% lower than the common steel density. This is because 1 wt.% Al addition produce 1.3% density reduction and in this class of steel high concentration of Al is present [6,7]. On the other hand, Al is a ferrite promoter and this effect is counterbalanced by Mn and C addition in order to maintain a volume fraction of austenite that can assure good ductility and toughness by the exploitation of twinning plasticity effect.

As a function of the balance between the ferrite and austenite promoters, the steels show different microstructures featured by different volume fractions of ferrite and austenite. On the basis of different microstructures, different combination of mechanical properties can be achieved. Ferritic steels have low amount of Mn and C and they can reach an ultimate tensile stress (UTS) of 200–600 MPa associated with a tensile elongation at fracture (TE) of 10–40%. On the contrary, a slightly higher concentration of Mn and C induces a duplex microstructure featured by the coexistence of ferrite and austenite that can reach UTS values of 400–900 MPa and a further increase of Mn and C induces a fully austenitic microstructure and UTS can reach 800–1300 MPa and TE of 30–80% [6].

One of the most important features in Fe–Mn–Al–C steel is the presence of κ-carbide phase. These carbides have a perovskite crystal structure designated as $E2_1$ and their stoichiometric formula is $(Fe,Mn)_3AlC$. However, also a metastable phase with a formula $(Fe,Mn)_3AlC_x$ ($x < 1$) has been experimentally verified [8] and its microstructure is usually indicated as $L'1_2$ or k'.

These carbides could be formed from austenite discontinuous precipitation (DP: $\gamma \rightarrow \gamma_0 + \alpha$, where γ_0 is carbon depleted austenite), precipitation transformation (PT: $\gamma \rightarrow \gamma_0 + \kappa$) and cellular transformation (CT: $\gamma \rightarrow \alpha + \kappa$ or $\gamma \rightarrow \alpha + \kappa + \gamma_0$) [9,10] or from spinodal decomposition of austenite (SD: $\gamma \rightarrow \gamma' + \gamma''$ $\rightarrow \gamma'$ + Short Range Ordered phase $\rightarrow \gamma' + \kappa'$) [11] or precipitation reaction at the grain boundaries of ferrite and austenite [12–15]. Due to the lattice structure very similar to austenite, κ-carbides appear coherent with austenite with a lattice parameter mismatch of 3% and semi-coherent with ferrite with a mismatch of almost 6% [6,11,16]. According to their shape, size and location they can have different effects as they can induce strengthening as well as embrittlement effects [14,17–19].

In steels showing a ferritic microstructure, κ-carbides are semi-coherent and are usually featured by a coarse and elongated rod-like shape and they are likely present at grain boundary affecting their strength [12].

In steels featured by the presence of austenite, κ-carbides can be observed as intragranular κ′-carbides or intergranular κ*-carbides. Fine intragranular κ′-carbides phase is considered to produce positive strengthening effects, increasing the yield strength [20–22], on the contrary intergranular κ*-carbides is much coarser and they can result in a severe loss in ductility [21,23].

Intragranular κ′-carbides are only present in steels with austenitic structure, they precipitate homogeneously in austenitic grains. They are coherent with the matrix and are featured by the metastable composition $(Fe,Mn)_3AlC_x$ ($x < 1$) [6].

Intergranular κ*-carbides are κ-precipitates formed at austenite grain boundaries. During ageing, after long annealing time κ*-carbides are found heterogeneously on the γ/γ grain boundaries in the form of coarse particles [6].

Fine intragranular carbides has been found to form during quenching or aging process in a short time range, but if the aging time is increased, the κ*-carbides at first form at γ grain boundaries and then they grow inside the austenite grains [11,24].

Because of their heterogeneous position along the grain austenite boundaries and of their morphology, κ*-carbides induce severe brittle behaviour, affecting the material mechanical response during hot-working, cold-working and under service condition at room temperature (RT) [13,25,26].

Thus, as a consequence of the importance of the role covered by the precipitation of those compounds, the study of their formation kinetics has been conducted by TTT experiments at different temperature and holding times.

In this paper are reported new results about effect of thermal treatments on κ-carbide precipitation kinetics in lightweight steel alloys. In addition, the implementation of

Table 1 – Chemical composition of the tested steels.

Mn (wt.%)	Al (wt.%)	C (wt.%)
10	9	0.4
10	9	1
10	12	0.4
20	12	0.4
20	12	1
30	12	0.4
30	12	1

Table 2 – Dino etching reagents list.

Quantity	Elements
140 ml	Distilled water
100 ml	Hydrogen peroxide (H_2O_2 30%)
4 g	Oxalic acid ($C_2H_2O_4 - 2H_2O$)
2 ml	Sulphuric acid (H_2SO_4)
1.5 ml	Hydrofluoric acid (HF)

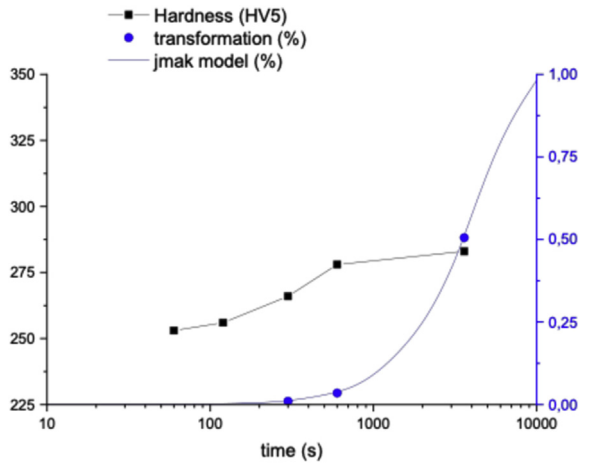

Fig. 1 – Transformation diagram for 10Mn 9Al 0.4C alloy at 600 °C.

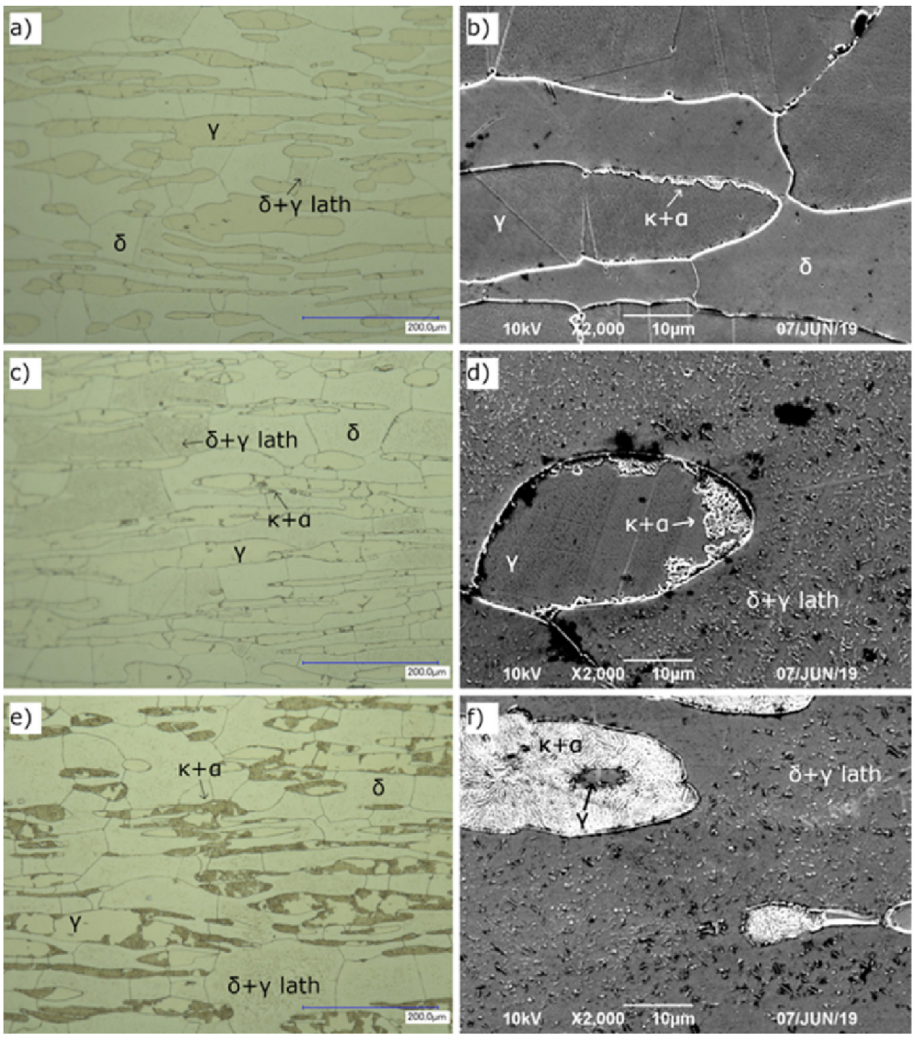

Fig. 2 – Microstructure of 10Mn 9Al 0.4C alloy samples treated at 600 °C for (a,b) 5min, (c,d) 10min and (e,f) 60min. a,c,e optical microscope images, b,d,f SEM images.

the JMAK model and the observation of a relationship between the chemical composition and the transformation activation energy are discussed.

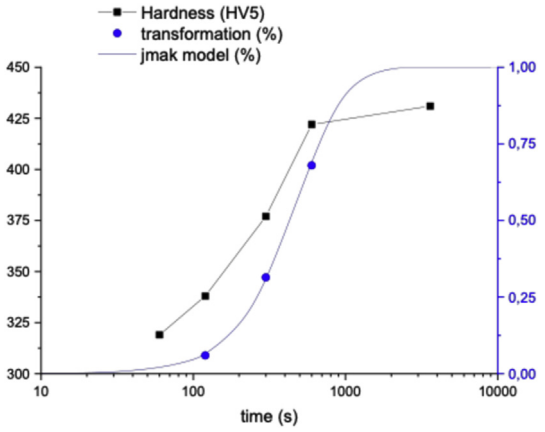

Fig. 3 – Transformation diagram for 10Mn 9Al 1C alloy at 600 °C.

2. Experimental procedure

2.1. Alloys

Steels featured by a combination of 10–20-30% Mn, 9–12% Al, 0.4–1% C concentrations have been chosen. A high concentration of Al is present in these compositions because the alloys studied have been designed to have a density almost 10% lower than the common steel, while Mn and C have to balance the ferritic promotion effect of Al in order to limit the ferrite content in the forecast duplex structures. The target chemical composition is presented in Table 1.

The tested material has been cast and hot rolled to a thickness of a 5 mm and quenched to room temperature after rolling. The casting and hot rolling operations has been performed in ArcelorMittal Global R&D - OCAS NV site in

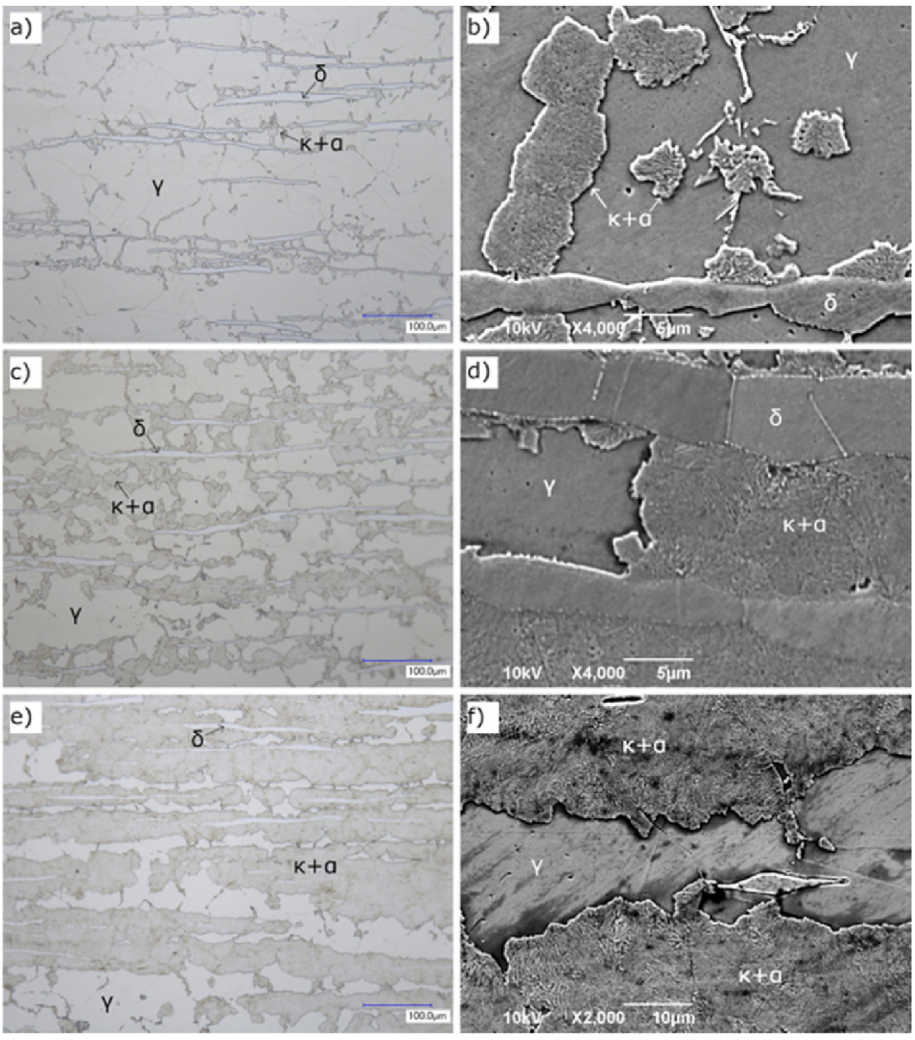

Fig. 4 – Microstructure of 10Mn 9Al 1C samples treated at 600 °C for (a,b) 2min, (c,d) 5min and (e,f) 10min. a,c,e optical microscope images, b,d,f SEM images.

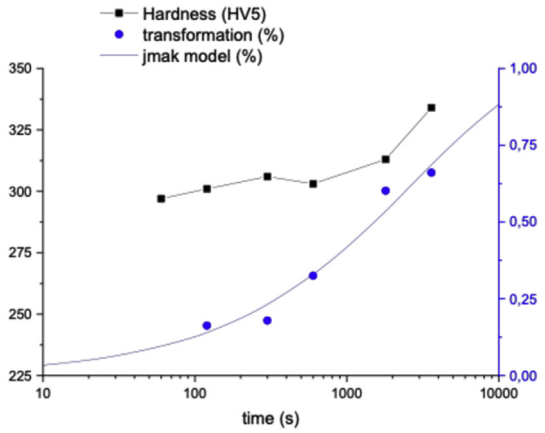

Fig. 5 – Transformation diagram for 10Mn 9Al 1C alloy at 800 °C.

Zwijnaarde, Gent (BE). The samples have been cut parallel to rolling direction from the hot rolled metal-sheet into samples featured by a size of 15 x 10 × 5 mm, in order to be heat treated in the furnace. Other samples have been cut into samples of 10 x 5 × 2 mm size, in order to be used in the dilatometer.

2.2. *Thermal treatments*

Samples have been treated at two different temperatures (600 and 800 °C) for different isothermal holding times (1, 2, 5, 10min and 1 h). Thermal treatments at 600 and 800 °C are performed with such holding times as the kinetics has been expected to be moderately fast but in some case additional treatments at 600 °C featured by holding times of 1-2-8-24 h have been performed to study the transformation up to the end. An additional test with holding time of 30min at 600 °C was performed for 20Mn 12Al 0.4C steel and at 800 °C for 10Mn 9Al 1C steel.

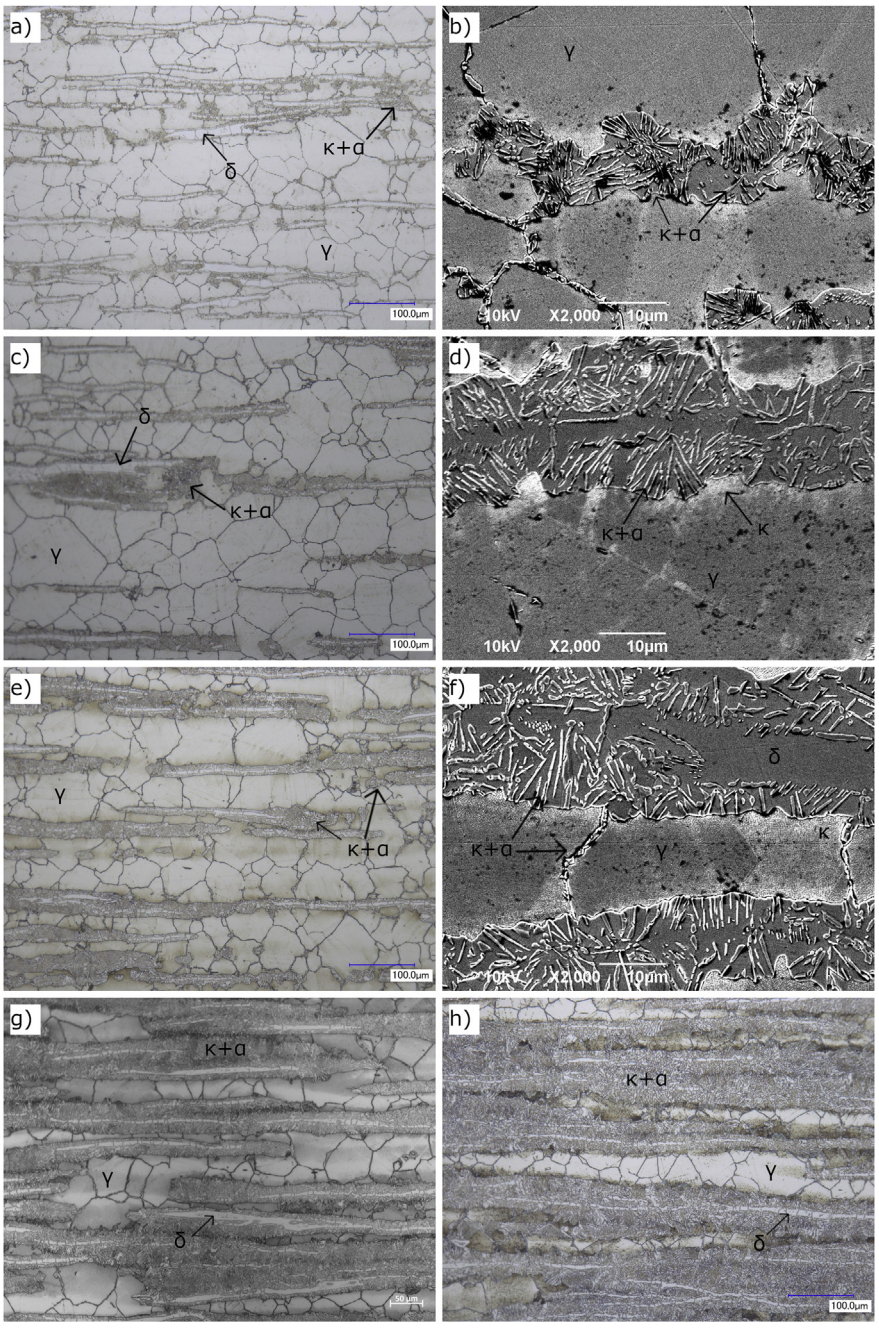

Fig. 6 – Microstructure of 10Mn 9Al 1C samples treated at 800 °C for (a,b) 2min, (c,d) 5min, (e,f) 10min, (g) 30min and (h) 60min. a,c,e,g,h optical microscope images, b,d,f SEM images.

© Bahr 805 Dilatometer and © Nabertherm 1280 °C - laboratory furnace have been employed for performing the tests.

2.3. *Sample preparation*

The grinding process of the sample has been performed by water cooled silicon-carbide papers starting from 200 μm roughness reaching 10 μm. The polishing process was carried out by polishing cloth disc and diamond-suspension lubrification and in two steps it was possible to reach the roughness of 3 μm, first, and then 1 μm.

Then the samples have been chemically etched using Dino etching, whose acid solution composition is reported in Table 2 and an exposure to the chemical solution of almost 10s has been applied.

2.4. *Hardness analysis*

Macro-hardness of the treated samples has been tested through Vickers method, applying a load of 5 kg. For each sample 5 indentations at the ¼ of the thickness have been performed.

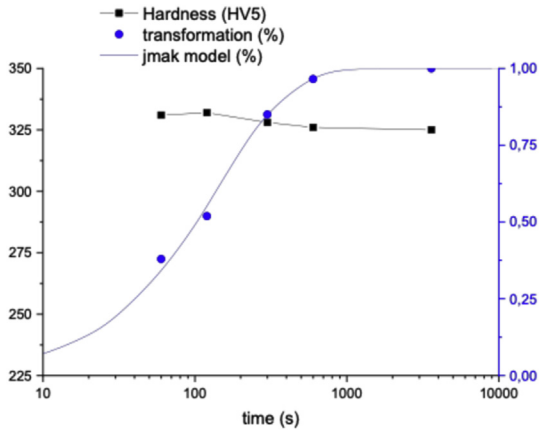

Fig. 7 – Transformation diagram for 10Mn 12Al 0.4C alloy at 800 °C.

2.5. *Microstructure analysis*

The samples have been examined by optical microscopes (OM) to obtain a correct view of the sample microstructure and in a scanning electron microscope (SEM) equipped with back scattered electron images (BSEI) and energy dispersive X-rays spectroscopy (EDXS) in order to examine the most interesting microstructural features. Through secondary electron images (SEI) the microstructural features at micro-sized and nano-sized scale have been examined and with the used of EDXS it was possible to correlate such feature to the steel micro-structural phases.

3. Results

From the microstructure observation, information about the phases and their relative amount have been obtained. On the basis of observations of the same alloy samples treated at the same thermal treatments temperature but applying progressively longer holding times, the relation between the fraction of transformed phase and the treatments time has been pointed out and the transformation kinetics has been defined.

The experimental data have been plotted and fitted with a curve featured by the expression given from the JMAK model [27,28]:

$$Y = 1 - \exp(-kt^n) \quad (1)$$

where Y is the transformed phase volume ratio; t is the time in s; k is a parameter associated with nucleation and growth rate of the transformed phase; n is a parameter related to the transformation directionality and nucleation and it can vary between 1 and 4.

The volume fraction of transformed phase has been considered equal to the microscope image surface fraction of the transformed phase, as the difference between the value of the surface and volume fraction is not significant. The transformed phase ratio has been obtained considering the ratio between the surface of the experimentally detected transformed phase ($\kappa+\alpha$) and the surface of austenite, which is the structural constituent that transforms to produce the precipitation of the transformed phase.

For each alloy, the transformation kinetic curve (Figs. 1, 3, 5, 7, 9, 11, 13 and 15) and the relative microstructure images (Figs. 2, 4, 6, 8, 10, 12, 14 and 16) have been reported.

Starting from 10Mn 9Al 0.4C alloy steel, thermal treatments carried out at 600 °C where effective resulting in a $\gamma \rightarrow \alpha+\kappa$ transformation of the microstructure starting after 5min of holding time (Fig. 2 a, b). After 60min holding time, the transformation has not been fulfilled (as visible in Fig. 2 e) but longer treatments have not been carried out.

In addition, the hardness increase during the transformation is limited (Fig. 1).

Steel 10Mn 9Al 1C thermally treated at 600 °C points out a sharp $\gamma \rightarrow \alpha+\kappa$ transformation (Fig. 4) that takes place for short holding time: less then 3600s as visible in Fig. 3.

Thermal treatment performed at 800 °C causes a net transformation, but in this case the transformed phase looks different and featured by thicker κ-carbides lamellae and it is clearly anticipated by spinodal decomposition (Fig. 6). Furtherly, it is possible to recognize δ grains becoming finer and this indicates that a transformation $\delta (\rightarrow \gamma) \rightarrow \kappa+\alpha$ goes on as the holding time increases.

The hardness increases after both the treatments but the values reached with treatments at 600 °C (Fig. 3) are much higher than the one observed with treatments at 800 °C (Fig. 5).

The steel 10Mn 12Al 0.4C points out $\gamma \rightarrow \alpha+\kappa$ transformation after treatments at both 600 and 800 °C, but a faster kinetics is caused by the treatment performed at 800 °C (Fig. 7). The transformation taking place at 800 °C is almost fulfilled after holding time of 600s (as visible in Fig. 8 e and g) while at 600 °C the first evident trace of transformation is visible only after 3600s and so it was not possible to measure it. The transformation recorded does not affect the hardness as visible in Fig. 7. The hardening effect given by the carbide precipitation has been neutralized by a softening mechanism such as the accommodation of internal stresses or dislocations present in the matrix.

Steel 20Mn 12Al 0.4C points out a cellular transformation visible only for treatments performed at 800 °C and for holding times between 600 and 3600s (Fig. 10). The lack of transformation after treatments at 600 °C is also confirmed by no increase of hardness while after treatments at 800 °C, after a limited decreasing trend, an increase even if limited has been recorded (Fig. 9).

Steel 20Mn 12Al 1C points out a cellular transformation at 800 °C that is anticipated by a spinodal decomposition (presence of κ' in Fig. 12 b and d) and it was possible to measure this ongoing transformation clearly visible at optical microscope (Fig. 12 a, c, e).

In Fig. 12 it was possible to distinguish κ' from κ on the basis of morphology criterion. According to the literature [6,20–23] κ′ carbides are embedded in austenite matrix as they have precipitated inside the austenite itself. On the contrary, κ carbides formed at the grain boundaries and for this reason and for the coarser shape they can be distinguished from κ′ carbides.

After treatments performed at 600 °C no microstructural change is observed even if equilibrium diagram establishes a microstructure different to the one observed:

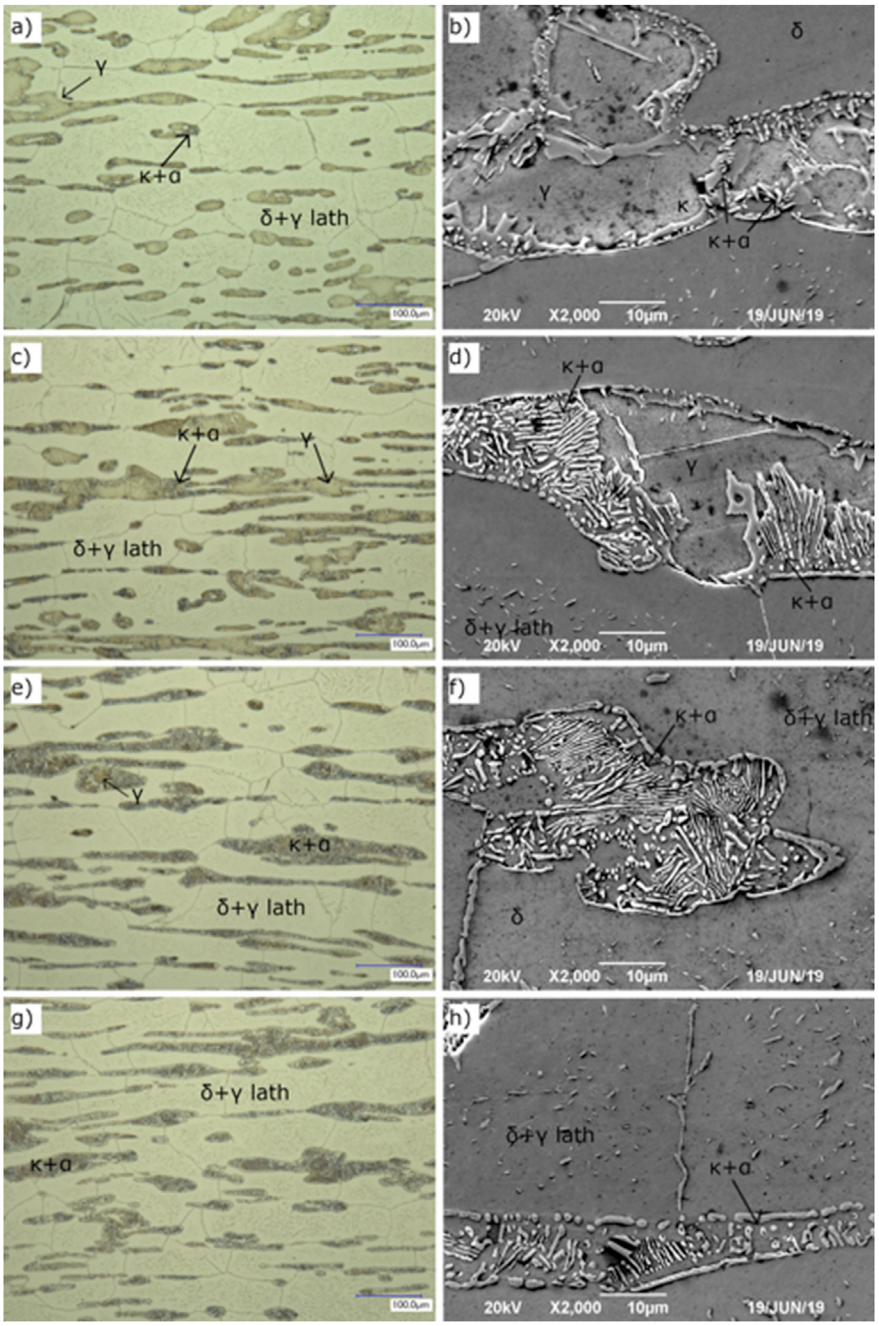

Fig. 8 – Microstructure of 10Mn 12Al 0.4C samples treated at 800 °C for (a,b) 1min, (c,d) 2min, (e,f) 5min and (g,h) 10min. a,c,e,g optical microscope images, b,d,f,h SEM images.

ferrite and κ-carbide are observed instead of austenite and ferrite.

After heat treatment at 800 °C only a slight increase of hardness has been recorded from 375 to 390 HV5 (Fig. 11), despite the clear transformation that has been observed.

Steel 30Mn 12Al 0.4C points out a cellular transformation of $\gamma \rightarrow \kappa + \alpha$ that has been taken place in samples treated at 600 °C for holding time longer than 3600s (Figs. 13 and 14). At the same temperature almost simultaneously a formation of $\alpha + \kappa$ lamellar structure in the δ-grain is visible (Fig. 14). This structure grows from grain boundary and consumes the whole δ-grain volume. Such $\alpha + \kappa$ lamellar structure provides a significant increase of the measured hardness values (Fig. 13), reaching values of 739 HV5.

Steel 30Mn 12Al 1C shows a clear transformation $\gamma \rightarrow \kappa + \alpha$ in the lamellar structure after heat treatment at 600 °C and the structure grows from γ phase grain boundary (Fig. 16). As a consequence of C concentration increase, the volume fraction of γ phase is much higher than in the previous cases. In this case hardness values are even higher than in the previous cases and reach the maximum of 777 HV5 (Fig. 15).

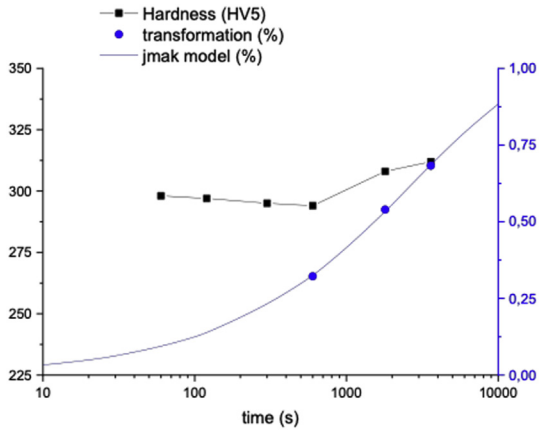

Fig. 9 – Transformation diagram for 20Mn 12Al 0.4C alloy at 800 °C.

The samples treated at 800 °C after short holding time (300s) show spinodal decomposition probably anticipating a cellular transformation, but such transformation is visible just at γ grain boundary only after treatments featured by holding times longer than 3600s and so it was not measured.

The JMAK model has been applied to state the relation between the chemical composition and the energy required for the transformation to happen. JMAK model is usually employed in static recrystallization (SRX) and in dynamic recrystallization (DRX) modelling [27] and in this case the parameter $t_{50\%}$ (time of half transformation) has been highlighted. Such parameter depends on temperature and on an activation energy according to an Arrhenius-like dependency. The different expression of the Avrami equation and the dependence of $t_{50\%}$ on an Arrhenius-like equation [27] is reported in Eqs. (2) and (3).

$$Y = 1 - \exp\left(-0,693 \cdot (t/t_{50\%})^{n'}\right) \quad (2)$$

$$t_{50\%} = k' \cdot \exp\left(-Q/RT\right) \quad (3)$$

In these equations, $t_{50\%}$ is the time at which the transformation is at the 50% of its progress. k' Summarizes the constants and parameters used for SRX (static recrystallization) or DRX (dynamic recrystallization) studies [27] and it

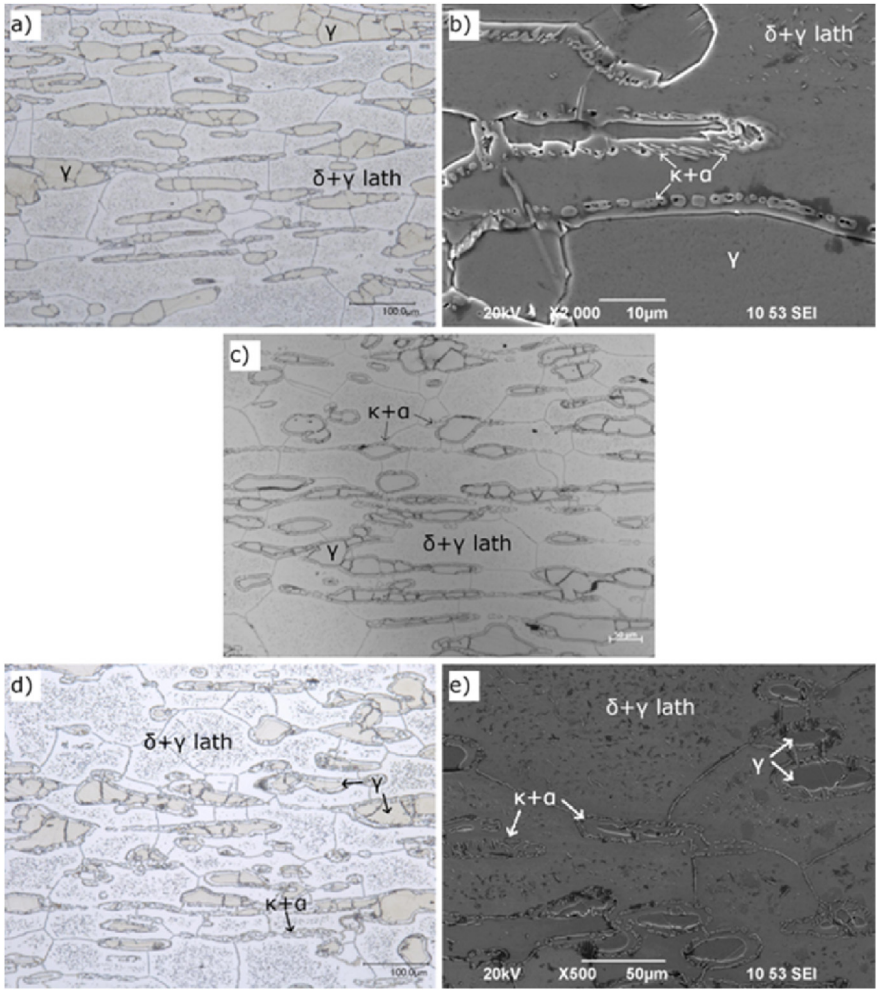

Fig. 10 – Microstructure of 20Mn 12Al 0.4C samples treated at 800 °C for (a,b) 10min, (c) 30min and (d,e) 60min. a,c,d optical microscope images, b,e SEM images with different magnification.

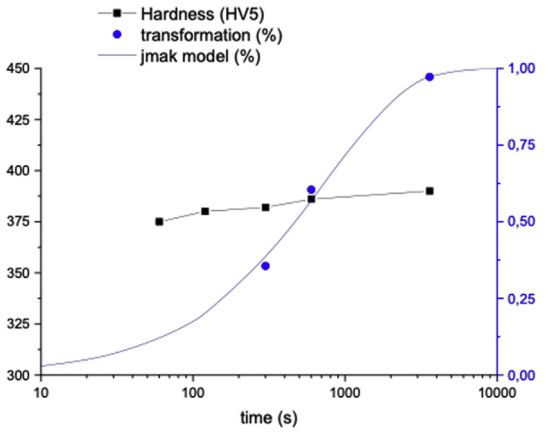

Fig. 11 – Transformation diagram for 20Mn 12Al 1C alloy at 800 °C.

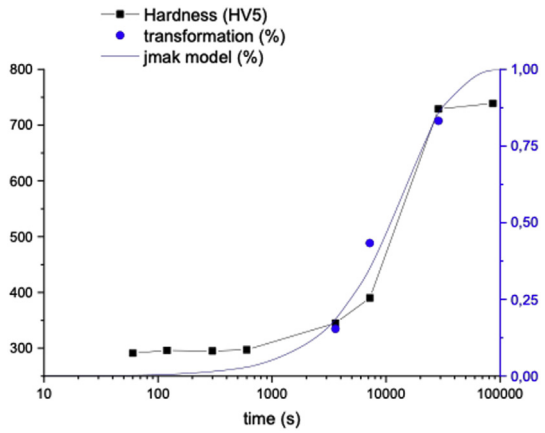

Fig. 13 – Transformation diagram for 30Mn 12Al 0.4C alloy at 600 °C.

depends on different parameters such as deformation rate or deformation energy activation.

The use of Eqs. (2) and (3) is aimed at finding a relation between the activation energy, present in the Arrhenius-like

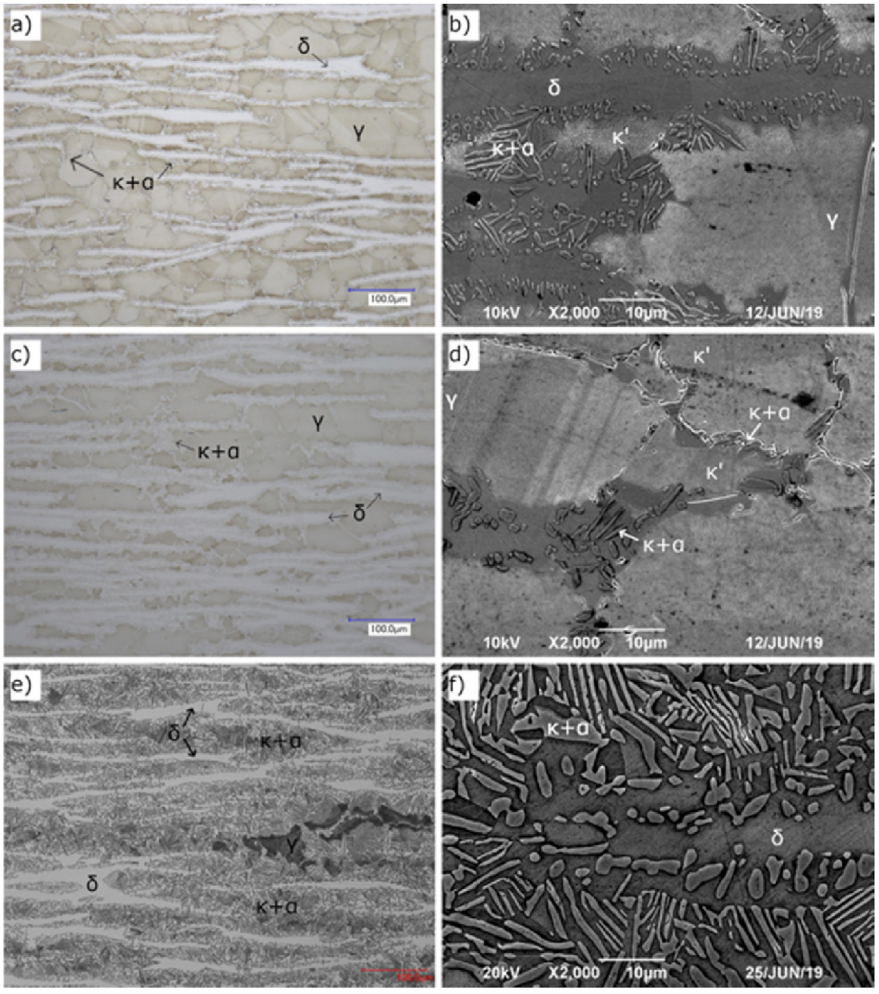

Fig. 12 – Microstructure of 20Mn 12Al 1C samples treated at 800 °C for (a,b) 5min, (c,d) 10min and (e,f) 60min. a,c,e optical microscope images, b,d,f SEM images.

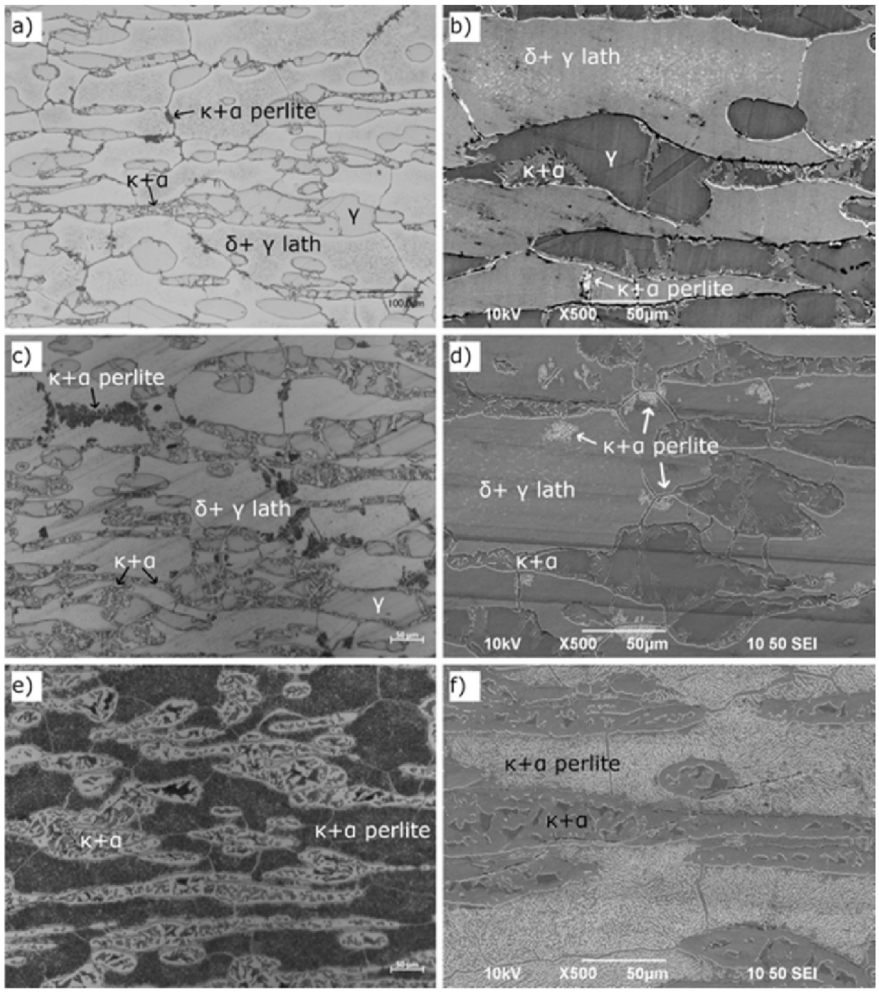

Fig. 14 – Microstructure of 30Mn 12Al 0.4C samples treated at 600 °C for (a,b) 1 h, (c,d) 2 h and (e,f) 8 h. a,c,e optical microscope images, b,d,f SEM images.

Eq. (3), and the chemical composition of these steels, assuming a linear relation such as the one presented in Eq. (4):

$$-Q / R = k_1 + k_2 \cdot Mn\% + k_3 \cdot Al\% + k_4 \cdot C\% \quad (4)$$

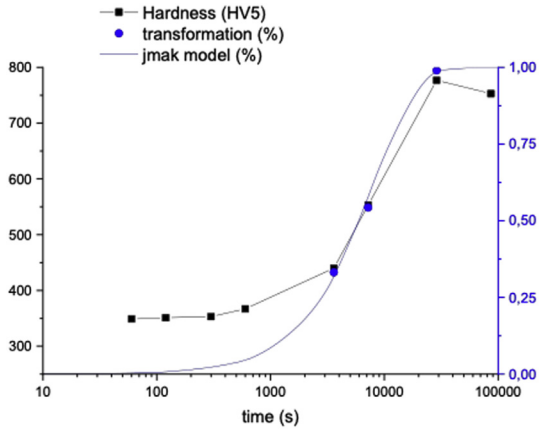

Fig. 15 – Transformation diagram for 30Mn 12Al 1C alloy at 600 °C.

It is possible to identify k_{i-th} coefficients using the steels' real chemical composition data (Table 3) rearranged in the expression of the JMAK model.

The results of such calculation are listed in Table 4. They were obtained using R© multi linear fitting.

It is possible to compare the effects of different elements and observe some clear trends.

Al and C addition significantly affect the Q/R and induce the same trend, while Mn points out a lower influence on the activation energy values and in addition it affects the values in a contrary way if compared to Al and C.

4. Discussion

Cellular transformations have been measured after treatments at 600 °C for 10Mn 9Al 0.4C, 30Mn 12Al 0.4C and 30Mn 12Al 1C alloys and after treatments at 800 °C for 10Mn 12Al 0.4C, 20Mn 12Al 0.4C and 20Mn 12Al 1C, while for 10Mn 9Al 1C the measurement of transformations have been performed after treatments at both temperatures. Except for the alloy containing 10%wt of Mn, the transformation occurred after

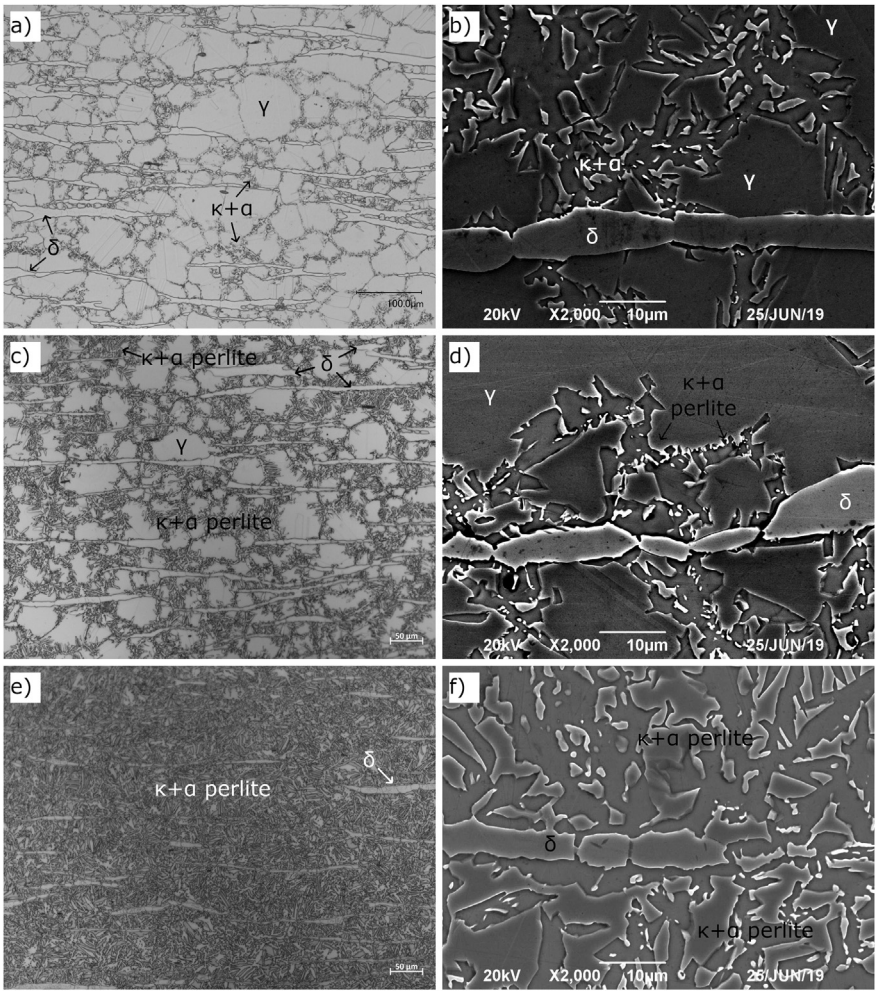

Fig. 16 – Microstructure of 30Mn 12Al 1C samples treated at 600 °C for (a,b) 1 h, (c,d) 2 h and (e,f) 8 h. a,c,e optical microscope images, b,d,f SEM images.

treatments at 600 °C point out a slower kinetics if compared to the transformation at 800 °C: The expected transformation has been detected only after long holding times (for 10Mn 12Al 0.4C alloy) or even no starting point are visible for the applied holding times (in the cases of steel 20Mn 12Al 0.4C and 20Mn 12Al 1C alloys). The observed transformation for 30Mn 12Al 0.4C and 30Mn 12Al 1C alloys have been observed only for very long holding times and this indicates that high concentration of Mn may indeed slow down the transformation kinetics. On the contrary an increase of Al and C concentration speeds up the transformation as a consequence of their increase of driving force ruling the κ-carbide precipitation.

The JMAK model analysis points out that the n values (Fig. 17) are close to 1 for almost all the compositions while for the transformation at 600 °C of 10Mn 9Al 0.4C and 10Mn 9Al 1C steels n is closer to 2. According to the JMAK theory, n has a physical meaning: $n = 1$ it is correlated to a non-random growth from a surface, while $n = 2$ is usually correlated to a growth from an edge [28]. Such low n values represent a very

Table 3 – Tested alloy real chemical composition.

Real Chemical Composition		
Mn	Al	C
10.18	9.28	0.4035
10.19	9.38	0.8588
10.10	11.92	0.3929
19.93	11.95	0.4153
20.10	12.20	0.8813
29.40	11.80	0.3876
29.30	11.70	0.9164

Table 4 – Coefficient Results from R© software.

Equation coefficient	Value	Variables
k_1	8608.89	Intercept
k_2	294.98	Mn %
k_3	−1625.75	Al %
k_4	−2122.95	C %

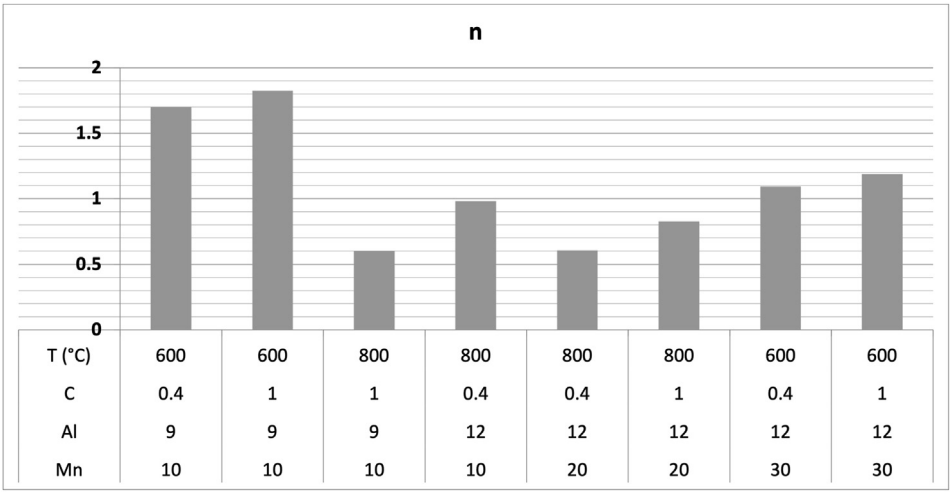

Fig. 17 – n values results.

high directionality in the transformation and a high concentration of constrained nucleation sites.

It is possible that the n values far from 1 are representative of a mixed mechanism of growth and nucleation, that could better represent real materials [29].

The n value observed for the different samples varies as a function of the chemical composition and the applied thermal treatment, but it could be average to a value close to 1, meaning an overall transformation ruled as a non-random growth from a surface.

It is visible that all the transformations at 600 °C have higher *n* if compared to the transformation at 800 °C (Fig. 17).

5. Conclusions

In this paper cellular transformation was observed on samples of lightweight steel alloys treated at 600 and 800 °C as a function of different holding times. The transformation development has been observed and analysed by the JMAK model to study kinetics of microstructural transformation.

It was observed that generally the transformation observed after treatments at 800 °C had faster kinetics than the one obtained from treatment at 600 °C, but, on the other hand treatments at 600 °C provided higher hardness increase and higher maximum values in comparison with the treatments carried out at 800 °C.

The parameters of JMAK relation have been studied and the n values for the different alloys is visible in Fig. 17. In addition, a linear relation between the time of half transformation and the alloy chemical composition has been established (Eq. (4) and Table 4). It was proofed that an increase of C and Al concentration increases the transformation kinetics, instead an increase of Mn concentration slows the microstructural transformation.

Funding

This research did not receive any specific grant from funding agencies in the public, commercial, or not-for-profit sectors.

Declaration of Competing Interest

The authors declare that they have no known competing financial interests or personal relationships that could have appeared to influence the work reported in this paper.

Acknowledgement

Special thanks to *ArcelorMittal Global R&D — OCAS (Belgium)* for giving the opportunity to exploit its resources and for its fruitful collaboration with *Politecnico di Milano*.

REFERENCES

[1] Raabe D, Tasan CC, Olivetti EA. Strategies for improving the sustainability of structural metals. Nature 2019;575:64–74. https://doi.org/10.1038/s41586-019-1702-5.

[2] Dhingra R, Das S. Life cycle energy and environmental evaluation of downsized vs. lightweight material automotive engines. J Clean Prod 2014;85:347–58. https://doi.org/10.1016/j.jclepro.2014.08.107.

[3] Helms H, Lambrecht U. The potential contribution of lightweighting to reduce transport energy consumption. LCA Case Studies Light-Weighting of Vehicles 2006. https://doi.org/10.1065/lca2006.07.258.

[4] Yoshimasa F, Yasunobu N. High strength steel sheets for weight reduction of automobiles. 2019.

[5] Tucker R. Trends in automotive lightweighting. Met Finish 2013;111:23–5. https://doi.org/10.1016/S0026-0576(13)70158-2.
[6] Chen S, Rana R, Haldar A, Ray RK. Current state of Fe-Mn-Al-C low density steels. Prog Mater Sci 2017;89:345–91. https://doi.org/10.1016/j.pmatsci.2017.05.002.
[7] Acselrad O, Simao RA, Pereira LC, Achete CA, Kalashnikov IS, Silva EM. Phase transformations in FeMnAlC austenitic steels with Si addition. Metall Mater Trans 2002;33:3569–73. https://doi.org/10.1007/s11661-002-0345-5.
[8] Yao MJ, Dey P, Seol JB, Choi P, Herbig M, Marceau RKW, et al. Combined atom probe tomography and density functional theory investigation of the Al off-stoichiometry of κ-carbides in an austenitic Fe-Mn-Al-C low density steel. Acta Mater 2016;106:229–38. https://doi.org/10.1016/j.actamat.2016.01.007.
[9] Cheng WC. Phase transformations of an Fe-0.85 C-17.9 Mn-7.1 Al austenitic steel after quenching and annealing. J Occup Med 2014;66:1809–20. https://doi.org/10.1007/s11837-014-1088-7.
[10] Aaronson HI, Pande CS. A synthesis of mechanisms for initiation of the cellular (or discontinuous precipitation) reaction. Acta Mater 1998;47:175–81. https://doi.org/10.1016/S1359-6454(98)00335-8.
[11] Cheng W, Cheng C, Hsu C, Laughlin D. Phase transformation of the L12 phase to kappa-carbide after spinodal decomposition and ordering in an Fe–C–Mn–Al austenitic steel. Elsevier; 2015.
[12] Seol JB, Raabe D, Choi P, Park HS, Kwak JH, Park CG. Direct evidence for the formation of ordered carbides in a ferrite-based low-density Fe-Mn-Al-C alloy studied by transmission electron microscopy and atom probe tomography. Scripta Mater 2013;68:348–53. https://doi.org/10.1016/j.scriptamat.2012.08.013.
[13] Youb Han S, Yong Shin S, Lee S, Kim NJ, Kwak J, Chin K. Effect of Carbon Content on Cracking Phenomenon Occurring during Cold Rolling of Three Light-Weight Steel Plates n.d. https://doi.org/10.1007/s11661-010-0456-3.
[14] Youb Han S, Yong Shin S, Lee H, Lee B, Lee S, Kim NJ, et al. Effects of Annealing Temperature on Microstructure and Tensile Properties in Ferritic Lightweight Steels n.d. https://doi.org/10.1007/s11661-011-0942-2.
[15] Sohn SS, Lee B, Lee S, Kwak J. Effect of Mn Addition on Microstructural Modification and Cracking Behavior of Ferritic Light-Weight Steels. Springer n.d. https://doi.org/10.1007/s11661-014-2502-z.
[16] Lee S, Jeong J, Lee YK. Precipitation and dissolution behavior of κ-carbide during continuous heating in Fe-9.3Mn-5.6Al-0.16C lightweight steel. J Alloys Compd 2015;648:149–53. https://doi.org/10.1016/j.jallcom.2015.06.048.
[17] Gutierrez-Urrutia I, Raabe D. High strength and ductile low density austenitic FeMnAlC steels: simplex and alloys strengthened by nanoscale ordered carbides. Mater Sci Technol 2014;30:1099–104. https://doi.org/10.1179/1743284714Y.0000000515.
[18] Kimura Y, Handa K, Hayashi K, Mishima Y. Microstructure control and ductility improvement of the two-phase γ-Fe/κ-(Fe, Mn)3AlC alloys in the Fe-Mn-Al-C quaternary system. Intermetallics 2004;12:607–17. https://doi.org/10.1016/j.intermet.2004.03.010.
[19] Lu WJ, Zhang XF, Qin RS. κ-carbide hardening in a low-density high-Al high-Mn multiphase steel. Mater Lett 2015;138:96–9. https://doi.org/10.1016/j.matlet.2014.09.104.
[20] Rana R. Low-density steels. J Occup Med 2014;66:1730–3. https://doi.org/10.1007/s11837-014-1137-2.
[21] Frommeyer G, Brüx U. Microstructures and mechanical properties of high-strength Fe-Mn-Al-C light-weight TRIPLEX steels. Steel Res Int 2006;77:627–33. https://doi.org/10.1002/srin.200606440.
[22] Kim H, Suh D-W, Kim NJ. Fe–Al–Mn–C lightweight structural alloys: a review on the microstructures and mechanical properties. Sci Technol Adv Mater 2013;14:014205. https://doi.org/10.1088/1468-6996/14/1/014205.
[23] Kalashnikov I, Acselrad O, Shalkevich A, Pereira LC. Chemical composition optimization for austenitic steels of the Fe-Mn-Al-C system. J Mater Eng Perform 2000;9:597–602. https://doi.org/10.1361/105994900770345430.
[24] Chao CY, Hwang CN, Liu TF. Grain boundary precipitation behaviors in an Fe-9.8Al-28.6Mn-0.8Si-1.OC alloy. Scripta Mater 1996;34:75–81.
[25] Sohn S, Lee B, Lee S, materialia JK-A. Effects of aluminum content on cracking phenomenon occurring during cold rolling of three ferrite-based lightweight steel. 2013 [Elsevier n.d].
[26] Yong Shin S, Lee H, Youb Han S, Seo C, Choi K, Lee S, et al. Correlation of Microstructure and Cracking Phenomenon Occurring during Hot Rolling of Lightweight Steel Plates. Springer n.d. https://doi.org/10.1007/s11661-009-0081-1.
[27] Jonas J, Quelennec X, Jiang L, materialia ÉM-A. The Avrami kinetics of dynamic recrystallization. Elsevier; 2009 [n.d].
[28] Fanfoni M, Tomellini M. The johnson-mehl-avrami-Kolmogorov model: a brief review. Nuovo cim della soc ital di fis D - condens matter. At Mol Chem Physics, Biophys 1998;20:1171–82. https://doi.org/10.1007/BF03185527.
[29] Li X, Miodownik AP, Saunders N. Modelling of materials properties in duplex stainless steels. Mater Sci Technol 2002;18:861–8. https://doi.org/10.1179/026708302225004694.